Efficient Organic Photovoltaic Cells Based on Nanocrystalline Mixtures of Boron Subphthalocyanine Chloride and C_{60}

*Richa Pandey, Aloysius A. Gunawan, K. Andre Mkhoyan, and Russell J. Holmes**

The electrical and structural behavior of uniformly mixed films of boron subphthalocyanine chloride (SubPc) and C_{60} and their performance in organic photovoltaic cells is explored. Device performance shows a strong dependence on active-layer donor–acceptor composition, and peak efficiency is realized at 80 wt.% C_{60}. The origin of this C_{60}-rich optimum composition is elucidated in terms of morphological changes in the active layer upon diluting SubPc with C_{60}. While neat SubPc is found to be amorphous, mixed films containing 80 wt.% C_{60} show clear nanocrystalline domains of SubPc. Supporting electrical characterization indicates that this change in morphology coincides with an increase in the hole mobility of the SubPc:C_{60} mixture, with peak mobility observed at a composition of 80 wt.% C_{60}. Organic photovoltaic cells constructed using this optimum SubPc:C_{60} ratio realize a power conversion efficiency of (3.7 ± 0.1)% under 100 mW cm^{-2} simulated AM1.5G solar illumination.

1. Introduction

Organic photovoltaic cells (OPVs) have received considerable attention due to their potential low cost and compatibility with roll-to-roll processing.[1,2] The excitonic character of organic semiconductors necessitates the use of an electron donor–acceptor (D–A) heterojunction to realize efficient exciton dissociation and harvesting.[3] Power conversion efficiencies (η_P) exceeding 7% have been realized in single-cell OPVs based on a conjugated polymer donor and a fullerene acceptor.[4] The essential role of D–A film morphology in realizing high efficiency has been thoroughly examined in these systems, permitting continued optimization and enhancements in performance.[5–7] Interestingly, while there have been similarly focused studies involving organic small-molecule active materials,[8–15] none have examined the promising D–A system of boron subphthalocyanine chloride (SubPc) and C_{60}. This D–A pairing has received significant attention due to demonstrations of high open-circuit voltages (V_{OC}) and power conversion efficiencies.[16–19] In this work, we seek to correlate the structural and electrical properties of uniformly mixed films of SubPc and C_{60}. Film morphology and device performance are observed to vary significantly with the D–A composition of the mixed film. Even more interesting however is the observation of optimum efficiency in OPVs that are very C_{60}-rich in composition.

Organic semiconductors are often characterized by a short exciton diffusion length (L_D) that can limit the fraction of photogenerated carriers that reach the dissociating D–A interface and contribute to photocurrent.[20,21] One way to overcome this limitation is to use uniform mixtures of the donor and acceptor materials so that the dissociating interface lies within L_D of every photogenerated exciton. This arrangement permits efficient exciton dissociation throughout the active layer.[8,10,22,23] While an increase in the area of the dissociating interface may enhance the exciton diffusion efficiency, the use of a mixture can also increase the average separation between molecules of a particular species, potentially reducing the charge carrier mobilities.[24] A reduction in the electron and hole mobilities can hinder charge collection and limit the overall performance of a uniformly mixed OPV.[24,25] In such systems, the exciton diffusion and charge collection efficiencies must be simultaneously optimized in order to realize high efficiency.

In this study, we show that a uniform mixture of SubPc:C_{60} containing 80 wt.% C_{60} is characterized by efficient exciton diffusion and charge transport leading to a high overall device efficiency. Interestingly, in the archetypical copper phthalocyanine (CuPc):C_{60} system, optimum device performance is typically realized in mixtures containing ~50 wt.% C_{60}.[26,27] Here, mixtures of SubPc:C_{60} are characterized in terms of device performance, electrical transport, and film morphology. Optimized performance in C_{60}-rich mixed SubPc:C_{60} OPVs is found to originate from an improvement in charge transport due to a change in film morphology and SubPc crystallinity with changes in D-A composition.

2. Results and Discussion

2.1. Device Characterization

Figure 1 compares the current-density–voltage (J–V) characteristics for planar and mixed heterojunction OPVs both in the dark and under simulated AM1.5G solar illumination (134 mW cm^{-2}). The optimized planar architecture consists of 10 nm MoO_3/13 nm SubPc/35 nm C_{60}, while the optimized mixture contains a

---

R. Pandey, A. A. Gunawan, Prof. K. A. Mkhoyan, Prof. R. J. Holmes
Department of Chemical Engineering and
Materials Science
University of Minnesota
Minneapolis, Minnesota 55455, USA
E-mail: rholmes@umn.edu

DOI: 10.1002/adfm.201101948

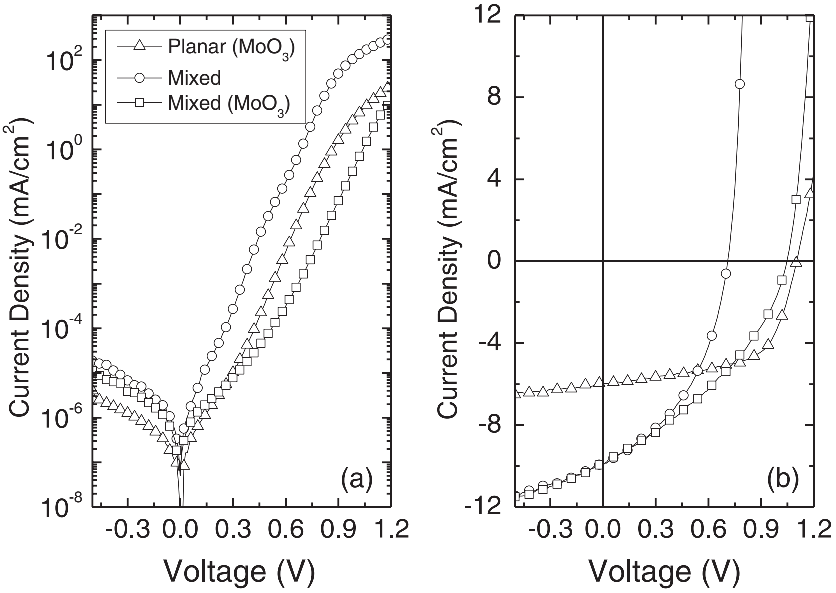

Figure 1. Current-density–voltage characteristics in (a) dark and (b) under simulated AM1.5G solar illumination at 134 mW cm^{-2} for a planar heterojunction OPV (13 nm SubPc/35 nm C_{60}) with a MoO_3 interlayer and mixed heterojunction OPVs (64 nm 80 wt.% C_{60}) both with and without a MoO_3 interlayer.

64-nm-thick layer of SubPc:C_{60} (80 wt.% C_{60}). Both structures are capped with a 10-nm-thick layer of the exciton blocking layer of bathocuproine (BCP).[28] Also shown in Figure 1 is the performance of a mixed device containing a 10-nm-thick layer of MoO_3 between the indium-tin-oxide (ITO) anode and the organic active layer. Under illumination, the mixed OPVs show comparable values of the short-circuit current density (J_{SC}). The inclusion of an MoO_3 interlayer in the mixed OPVs significantly reduces the dark current, leading to an increase in V_{OC} compared to devices with no interlayer.[29,30]

Figure 2 shows operating parameters for mixed SubPc:C_{60} OPVs containing either 50 wt.% C_{60}, 80 wt.% C_{60} or 90 wt.% C_{60}, with an MoO_3 interlayer as a function of the mixture thickness under simulated AM1.5G solar illumination at 100 mW cm^{-2}. The fill factor (*FF*) for all three mixed heterojunction OPVs decreases with increasing active layer thickness due to a reduction in the charge collection efficiency.[31] The C_{60}-rich mixtures show a significantly larger *FF* compared to OPVs containing 50 wt.% C_{60}. The *FF* for the 80 wt.% C_{60} mixture is the largest over all thicknesses, suggesting improved charge transport relative to the other mixtures. J_{SC} increases with thickness as a result of increasing optical absorption and decreases at high thicknesses due to a reduction in the charge collection efficiency and a saturation of the absorption efficiency.[29] V_{OC} does not show a strong dependence on the D–A composition ratio or on the active layer thickness. This is due to the use of

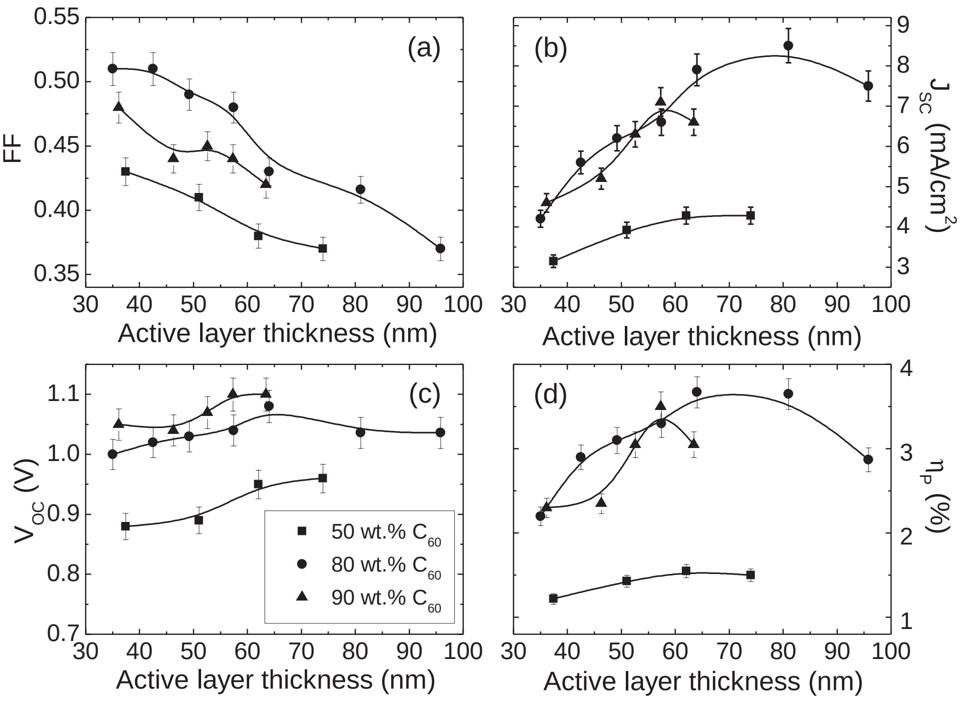

Figure 2. Photovoltaic operating parameters for mixed SubPc:C_{60} OPVs containing 50 wt.% C_{60}, 80 wt.% C_{60}, and 90 wt.% C_{60} at 100 mWcm^{-2} as a function of mixture thickness. a) Fill factor (*FF*), b) short-circuit current density (J_{SC}), c) open-circuit voltage (V_{OC}), and d) power conversion efficiency (η_P).

Table 1. Device parameters for optimized planar and mixed heterojunction OPVs under AM1.5G simulated solar illumination (100 mW/cm^2)

Device Structure	J_{SC} [mA cm^{-2}]	V_{OC} [V]	FF	η_P [%]
Planar	4.50	1.08	0.62	3.05
Mixed (50 wt.% C_{60})	4.30	0.95	0.38	1.55
Mixed (80 wt.% C_{60})	7.90	1.07	0.44	3.70
Mixed (90 wt.% C_{60})	7.10	1.10	0.44	3.44

electron and hole blocking layers of MoO_3 and BCP, respectively, which ensure a low dark current over all mixture compositions. The high FF and J_{SC} of mixed OPVs containing 80 wt.% C_{60} leads to a peak η_P of (3.7 ± 0.1)% at an active layer thickness of 64 nm. Relative to a planar heterojunction, this optimum mixture shows a higher exciton diffusion efficiency due to a larger D–A interface area leading to a ~75% increase in the J_{SC}, as shown in **Table 1**. In contrast, the planar heterojunction shows a significantly higher FF compared to the mixed OPVs. This is attributed to a reduced charge collection efficiency in the mixed heterojunction under forward bias. Overall, an increase in the exciton diffusion efficiency for an optimized mixed heterojunction OPV more than offsets the reduction in charge collection efficiency leading to a ~20% increase in the η_P compared to an optimized planar heterojunction OPV.

Figure 3a shows normalized absorption spectra for a neat film of SubPc and mixtures of SubPc:C_{60} containing either 50 wt.% C_{60}, 80 wt.% C_{60} and 90 wt.% C_{60}. Interestingly, a long wavelength tail extending from 650 to 750 nm is observed in the absorption of the mixed films. A similar feature in the near-infrared has been previously attributed to charge-transfer state absorption in mixtures of zinc phthalocyanine and C_{60}.[32]

Figure 3b compares the external quantum efficiency (η_{EQE}) of optimized planar and mixed OPVs. The optimum active layer thicknesses for mixtures containing 50 wt.% C_{60}, 80 wt.% C_{60} and 90 wt.% C_{60} are 62 nm, 64 nm, and 57 nm, respectively. The photoresponse occurring at short wavelengths originates mainly from C_{60} while the response at $\lambda \geq 500$ nm corresponds to absorption in SubPc. The long L_D of C_{60} likely leads to a high exciton diffusion efficiency for excitons created on C_{60} for all three compositions.[33,34] Improved charge transport combined with an increase in the absorption efficiency of C_{60} in moving from 50 wt.% C_{60} to 90 wt.% C_{60} leads to increased C_{60} response in the η_{EQE}. Even though the absorption efficiency of SubPc in a mixture containing 80 wt.% C_{60} is significantly lower than that of a mixture containing 50 wt.% C_{60}, the mixture containing 80 wt.% C_{60} shows the largest response from SubPc in the η_{EQE}. This reflects an improvement in the charge collection efficiency for mixed films containing 80 wt.% C_{60}, and also suggests that the internal quantum efficiency is maximized for excitons created on SubPc. The η_{EQE} of all three mixed OPVs shows the same long wavelength tail observed in Figure 3a as a result of charge-transfer state absorption.

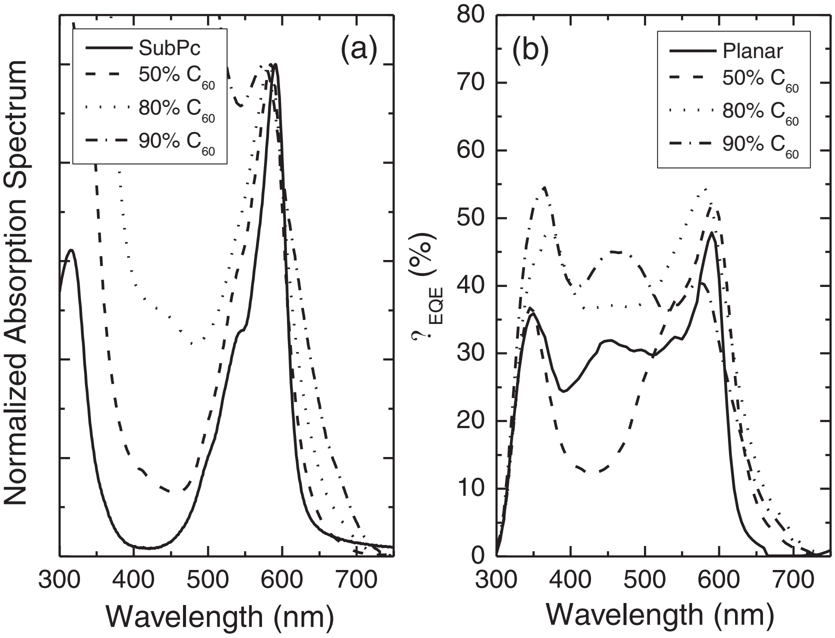

Figure 3. a) Normalized absorption spectra for neat SubPc and mixtures of SubPc:C_{60} as a function of composition. b) External quantum efficiency (η_{EQE}) spectra for a planar heterojunction OPV (13 nm SubPc/35 nm C_{60}) and mixed SubPc:C_{60} OPVs with active layers containing (thickness) 50 wt.% C_{60} (62 nm), 80 wt.% C_{60} (64 nm), or 90 wt.% C_{60} (57 nm).

2.2. Charge Transport in Mixtures of SubPc:C_{60}

In order to understand the observed trends in device performance as a function of composition, single carrier devices were used to extract the electron and hole mobilities. The current density-voltage characteristics for uniformly mixed electron- and hole-only devices were analyzed using a model of space-charge-limited current (SCLC).[35–37] In the absence of traps, the space-charge-limited current density (J) can be written as a function of the applied voltage (V) as[35]:

$$J = \frac{9}{8}\varepsilon\varepsilon_0\mu\frac{V^2}{d^3} \tag{1}$$

where ε_0 is the permittivity of free space, ε is the relative dielectric constant of the organic thin film, μ is the charge carrier mobility, and d is the organic film thickness. In this work, the relative dielectric constant is approximated as $\varepsilon = 4$.

In organic semiconductors, the charge carrier mobility often exhibits a Poole–Frenkel dependence on the electric field.[38,39] This functional dependence is attributed to a random variation in hopping site energies for disordered organic semiconductors, leading to energetic barriers for carrier transport that are overcome with an applied electric field.[40,41] In this case, the mobility can be expressed as:

$$\mu(E) = \mu_0 \exp[\gamma E^{1/2}] \tag{2}$$

where μ_0 is the zero-field mobility, γ is the field activation parameter, and E is the applied electric field. The electric field is approximated as constant over the active layer in order to extract both the zero-field mobility and field activation parameter from single-carrier current density-voltage characteristics. Current density–voltage characteristics for electron- and hole-only devices having a variety of mixture compositions were measured for organic film thicknesses of 150 nm, 200 nm, and 250 nm. The values of the extracted mobility and field activation parameter for each thickness were found to be within experimental error, confirming that the measured properties reflect the bulk behavior of the film. Hole-only devices were also fabricated with an MoO_3 interlayer. Hole mobility values measured with and without an MoO_3 interlayer were within experimental error, providing further evidence of bulk limited transport in single-carrier devices.

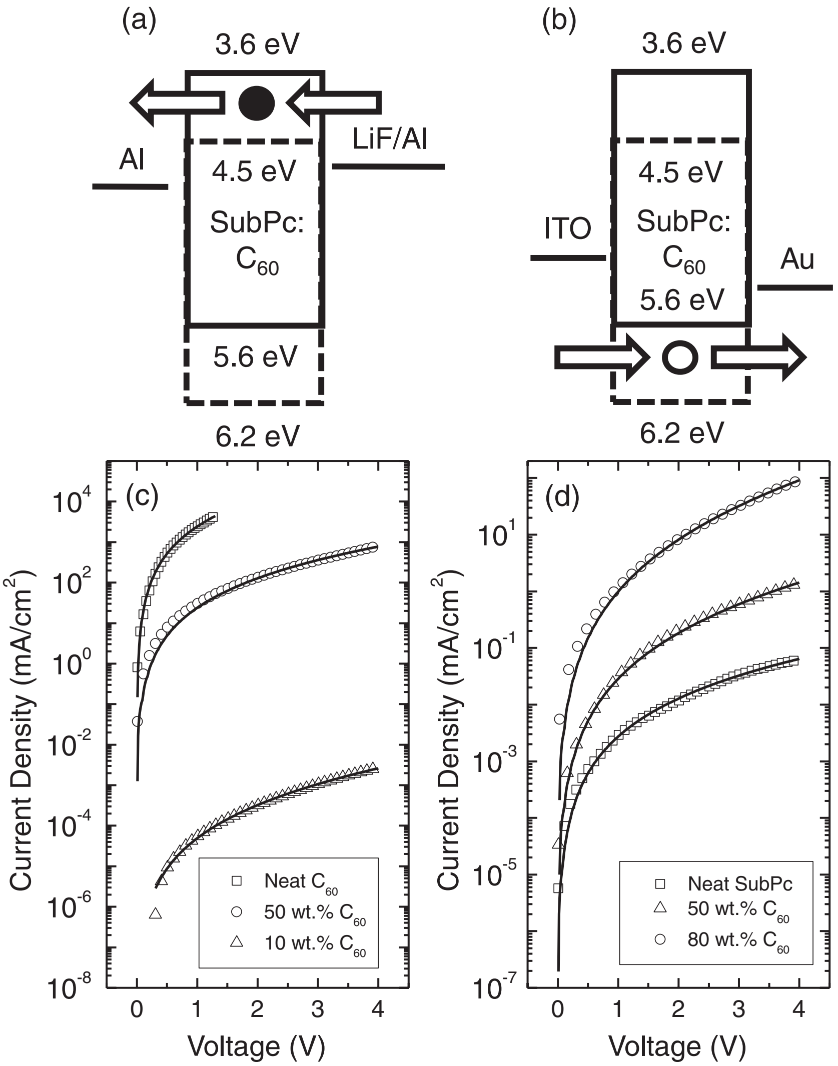

Figure 4. Molecular orbital energy level diagram for a SubPc:C_{60} mixture showing (a) electron transport along the lowest unoccupied molecular orbital (LUMO) of C_{60} and (b) hole transport along the highest occupied molecular orbital (HOMO) of SubPc. *J–V* characteristics for single-carrier devices containing a 200-nm-thick organic layer comprising of: c) neat C_{60}, 50 wt.% C_{60} (50 wt.% SubPc) and 10 wt.% C_{60} sandwiched between electrodes of Al and LiF/Al (electron-only); d) neat SubPc, 50 wt.% C_{60} and 80 wt.% C_{60} sandwiched between electrodes of ITO and Au (hole-only). The open symbols are experimental *J–V* characteristics for single carrier devices, while the solid lines are fits using the model discussed in the text.

Electron-only devices were fabricated to characterize electron transport in the mixture along molecules of C_{60}. These devices use an electron-injecting contact consisting of LiF/Al, and an electron-collecting contact of Al. It was observed that the electron current density using a LiF/Al cathode was almost three orders of magnitude larger than that obtained using an Al cathode, consistent with previous work on similar systems.[37] Hole transport along molecules of SubPc was characterized using hole-injecting and -collecting electrodes of ITO and Au. The molecular orbital energy level diagrams for both electron- and hole-only devices are shown in **Figure 4**a and b, respectively. Figure 4c and d shows fits to the electron-only and hole-only current density-voltage characteristics using Equations 1 and 2, with the corresponding fit parameters for various mixture compositions shown in **Table 2**. For a neat film of C_{60}, a zero-field electron mobility of $\mu_0 = (3.3 \pm 0.2) \times 10^{-2}$ cm^2 V^{-1} s^{-1} is extracted, which is in good agreement with values reported previously.[24] This high mobility is maintained to a composition of 80 wt.% C_{60} and decreases with a further reduction in the C_{60} composition (**Figure 5**). The distance between C_{60} molecules is likely increased upon dilution with SubPc leading to a reduction in the electron mobility for mixtures containing <80 wt.% C_{60}. The hole mobilities in neat films of SubPc and C_{60} were separately measured to be $\mu_0 = (4.5 \pm 2.3) \times 10^{-8}$ cm^2 V^{-1} s^{-1} and $\mu_0 = (2.8 \pm 1.4) \times 10^{-7}$ cm^2 V^{-1} s^{-1}, respectively. The measured value for C_{60} is in good agreement with those previously reported in the literature.[42] Interestingly, the hole mobility extracted for mixtures of SubPc:C_{60} is observed to increase by two orders of magnitude on increasing the C_{60} composition from 0 wt.% to 80 wt.%, and decreases with a further increase

Table 2. Parameters extracted from mixed SubPc:C_{60} single carrier devices.

Composition [% C_{60}]	Electron		Hole	
	μ_0 [cm^2 V^{-1} s^{-1}]	γ [cm V^{-1}]$^{1/2}$	μ_0 [cm^2 V^{-1} s^{-1}]	γ [cm V^{-1}]$^{1/2}$
0 (100% SubPc)	5.2×10^{-10}	1.2×10^{-3}	4.5×10^{-8}	1.8×10^{-3}
10	5.7×10^{-10}	5.3×10^{-3}	2.3×10^{-8}	6.0×10^{-3}
30	1.9×10^{-6}	1.0×10^{-3}	1.6×10^{-7}	2.2×10^{-3}
50	1.5×10^{-4}	2.9×10^{-3}	1.8×10^{-7}	5.1×10^{-3}
80	1.1×10^{-2}	4.2×10^{-3}	3.4×10^{-6}	4.8×10^{-3}
90	1.5×10^{-2}	4.6×10^{-3}	3.4×10^{-7}	7.6×10^{-3}
100	3.3×10^{-2}	2.4×10^{-3}	2.8×10^{-7}	4.4×10^{-3}

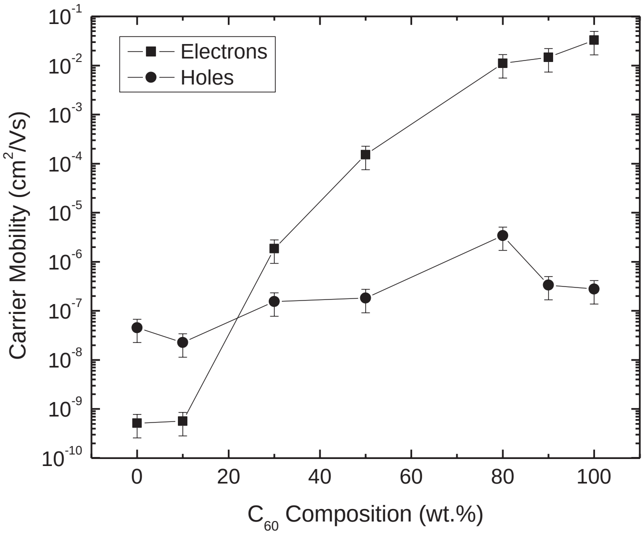

Figure 5. Zero-field mobility of electrons and holes in neat SubPc, neat C_{60} and various SubPc:C_{60} mixtures as a function of composition. All organic layers are 200 nm thick.

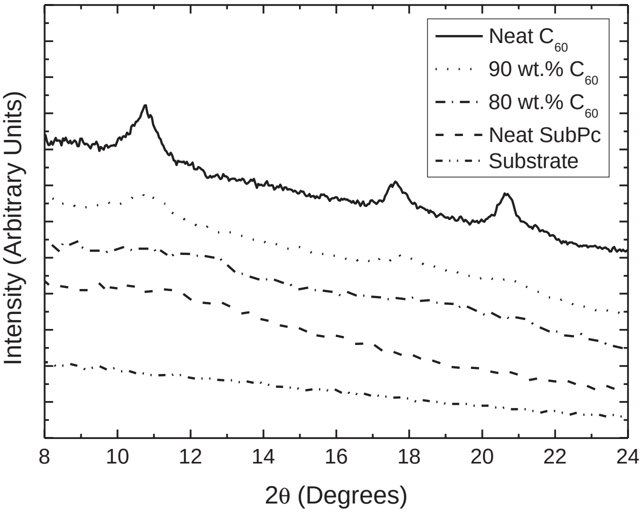

Figure 6. X-ray diffraction patterns for neat films of C_{60} and SubPc, as well as for mixtures of SubPc:C_{60} with varying composition. Also shown is the X-ray diffraction pattern for the Si wafer substrate. All spectra are measured in the θ–2θ geometry with Cu K_α radiation. All organic layers are 200 nm thick. The raw data has been offset for clarity.

in the C_{60} concentration (Figure 5). Similar behavior has been previously observed in blends of a conjugated polymer donor and fullerene acceptor.[36,37] In polymer blends, this increase is usually attributed to hole transport along the acceptor species or, is the result of improved molecular packing of the donor species upon addition of the fullerene acceptor. In this work, the potential for hole transport along molecules of C_{60} was ruled out by comparing the current density-voltage characteristics of a hole-only device containing a uniformly mixed film of SubPc:C_{60} with those of a hole-only device that also contained a 15-nm-thick hole-blocking layer of C_{60} between the mixed layer and the hole-collecting Au electrode. For devices containing a C_{60} blocking layer, the current density is reduced substantially, suggesting that hole transport in the mixture occurs along molecules of SubPc.

2.3. Film Morphology in Mixtures of SubPc:C_{60}

In order to characterize the morphology of neat and mixed layers of C_{60} and SubPc, X-ray diffraction (XRD) spectra were collected from 100-nm-thick organic films in the θ–2θ geometry with Cu K_α radiation ($\lambda = 1.54$ Å). **Figure 6** shows diffraction spectra obtained for neat films of C_{60} and SubPc, as well as for mixtures of varying composition. For a neat film of C_{60}, peaks are observed at diffraction angles of $2\theta = (10.7 \pm 0.1)°$, $(17.6 \pm 0.1)°$ and $(20.7 \pm 0.1)°$. These correspond to crystal lattice *d*-spacings of (8.3 ± 0.1) Å, (5.0 ± 0.1) Å and (4.3 ± 0.1) Å and the (111), (220) and (311) planes of C_{60}.[43,44] Diffraction peaks are indexed according to the face-centered cubic (FCC) structure of C_{60}. In contrast, a neat film of SubPc shows no diffraction peaks indicating that the film is amorphous, as noted in previous reports using similar growth conditions.[17,45] The C_{60} peaks in XRD are observed to weaken in intensity upon adding SubPc, and are barely resolved in a mixed film containing 90 wt.% C_{60}. Mixed films with 50 wt.% C_{60} and 80 wt.% C_{60} do not show evidence of substantial crystallinity for SubPc or C_{60}. While XRD is often utilized to determine the crystallinity of organic semiconductor thin films, substantial additional insight into the nanoscale morphology can be obtained using transmission electron microscopy (TEM).[5,43]

A series of TEM images (top view) for a neat film of C_{60}, as well as mixed films containing 90 wt.% C_{60}, 80 wt.% C_{60}, and 50 wt.% C_{60} were collected to further characterize the distribution of crystalline and amorphous regions (**Figure 7**). Rigorous TEM imaging was carried out both on Si (single crystal) substrates and carbon-grids (amorphous). Similar morphology was observed in both cases suggesting that the observed film morphology is independent of the underlying substrate. A neat film of C_{60} (Figure 7a) exhibits a substantially crystalline network embedded in an otherwise amorphous matrix. The appearance of bright spots in the fast-Fourier transform (FFT) of a 8 nm × 8 nm region of the image (shown as inset figures) further highlights the presence of crystallinity. Upon adding 10 wt.% SubPc to C_{60} (Figure 7b), the crystallinity of C_{60} is reduced, consistent with the XRD results of Figure 6. Interestingly, upon adding 20 wt.% SubPc to C_{60}, the film shows clear nanocrystalline domains (Figure 7c). The FFT intensity maxima observed from the 80 wt.% C_{60} mixture are the strongest among all compositions investigated, indicating the presence of a crystalline phase in this mixture. The further addition of SubPc to construct a mixture containing 50 wt.% C_{60} (Figure 7d) reduces the crystalline content and the film becomes effectively amorphous. Separate TEM imaging of a neat film of SubPc exhibited no signatures of crystallinity, consistent with the XRD spectrum of Figure 6.

In addition to image analysis via FFT, selected-area electron diffraction (SAED) was also performed to determine the molecular constituent of the observed nanocrystalline regions. Quantifying the SAED data provides information regarding the *d*-spacing which can help to identify which component(s) of

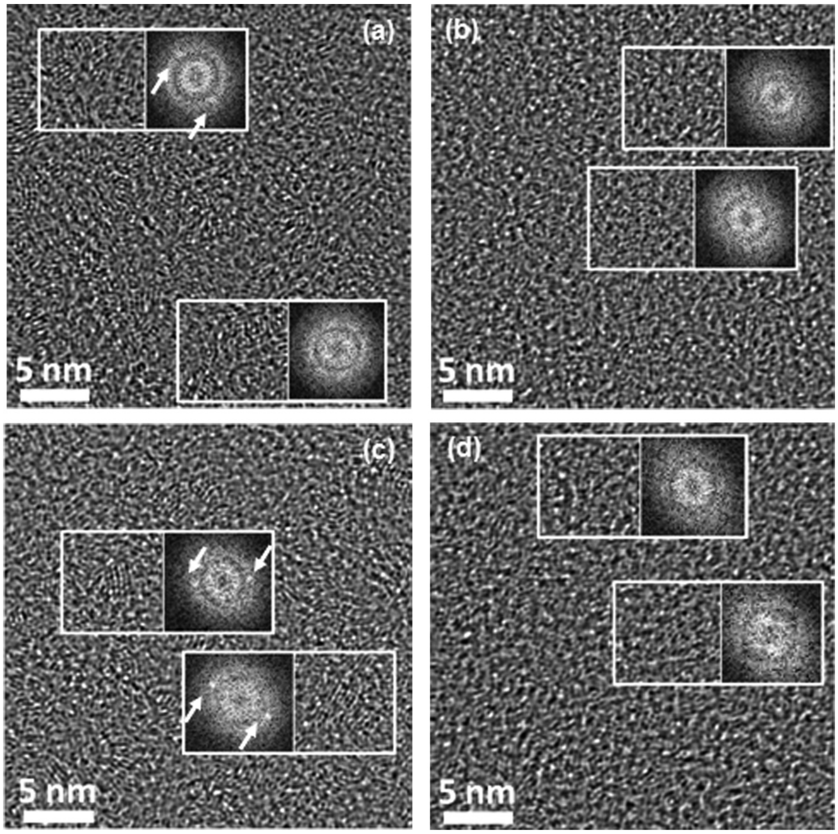

Figure 7. High-resolution TEM image (top view) for thin films containg (a) neat C_{60}, (b) 90 wt.% C_{60} (10 wt.% SubPc), (c) 80 wt.% C_{60}, and (d) 50 wt.% C_{60}. The insets show fast-Fourier transforms of the selected region of the corresponding image.

the mixture are contributing to the crystallinity. **Figure 8**a and b shows the SAED data obtained from neat C_{60} and 80 wt.% C_{60} films, respectively. The presence of well-defined rings in the diffraction pattern for neat C_{60} implies that the film is polycrystalline, consistent with the XRD data of Figure 6. Some of the polycrystalline phase of C_{60} is still retained at 90 wt.% with a reduced azimuthal intensity distribution indicative of small grains. In contrast to neat C_{60}, the diffraction pattern collected from films containing 80 wt.% C_{60} is characterized by high intensity spots scattered over a wide radial range. Figure 8c shows the comparison of *d*-spacings observed experimentally using SAED for neat C_{60} and mixed (80 wt.% and 90 wt.% C_{60}) films with the theoretically predicted *d*-spacings for SubPc and C_{60}. The three rings observed for electron diffraction from neat C_{60} correspond to the (111), (220) and (311) planes (FCC) in agreement with the XRD data of Figure 6. The same three planes are also observed in SAED spectra collected for mixed films containing 90 wt.% C_{60}. For mixed films containing 80 wt.% C_{60}, reflections corresponding to a *d*-spacing of 4.7 Å are observed that cannot be attributed to crystalline C_{60}. This *d*-spacing correlates well with the (220) plane of orthorhombic SubPc.[45,46] This analysis suggests the presence of nanocrystalline domains of SubPc in addition to C_{60} crystallinity in the mixed film containing 80 wt.% C_{60}. Given that the SAED measurement integrates over a circular area with a diameter of 5 μm, these results may suggest that the structure observed in Figure 7c consists of nanocrystalline domains of SubPc in a partially crystalline matrix of C_{60}. While the mechanism for the growth of crystalline SubPc in films containing 80 wt.% C_{60} requires further investigation, this phenomenon may be the result of crystal nucleation at the C_{60} surface. Interestingly, the observation of SubPc crystallinity requires a critical balance between SubPc and C_{60}, and is only observed at 80 wt.% C_{60}.

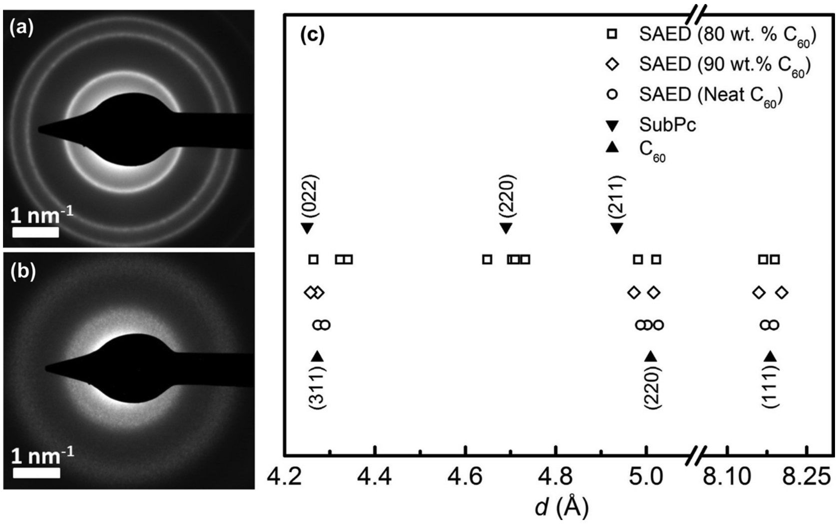

Figure 8. Selected area electron diffraction (SAED) patterns for thin films containing neat C_{60} (a) and 80 wt.% C_{60} (20 wt.% SubPc) (b). c) Experimentally determined *d* -spacings for the spectra of (a), (b), and 90 wt.% C_{60} and theoretically predicted values based on the crystal structures of SubPc and C_{60}.

2.4. Impact of Morphology on Charge Transport

Neat films of SubPc are amorphous and characterized by a low hole mobility. The construction of a uniformly mixed film containing 20 wt.% SubPc and 80 wt.% C_{60} leads to the formation of nanocrystalline domains of SubPc which likely exist through the depth of the mixture forming pathways for hole transport. The increase in SubPc crystallinity shown in Figure 7 correlates well with the observed increase in hole mobility for mixtures of SubPc:C_{60} upon the addition of C_{60}, peaking at a composition of 80 wt.% C_{60}. No significant SubPc crystallinity is observed in mixed films containing 90 wt.% C_{60}, leading to a reduction in the hole mobility upon further addition of C_{60}.

The presence of crystalline C_{60} in neat film and in mixtures of 90 wt.% C_{60} and 80 wt.% C_{60} likely permits a uniformly high electron mobility (Figure 8). This crystallinity is lost with a further reduction in the C_{60} composition, suggesting that mixtures with <80 wt.% C_{60} comprise essentially amorphous mixtures of SubPc and C_{60}. Correspondingly, the electron mobility is also noted to decrease significantly at these compositions. As such, a high C_{60} composition in the SubPc:C_{60} mixture leads to both high electron and hole mobilities and hence, effective charge transport in an OPV. This leads to a high FF and J_{SC} for OPV cells based on C_{60}-rich mixtures (Figure 2).

3. Conclusions

In conclusion, we have rigorously explored the electrical and morphological properties of mixed films of SubPc and C_{60}, the correlation between these properties, and the resulting device performance. While neat films of SubPc are amorphous, SubPc forms nanocrystalline domains in mixed film when C_{60} comprises 80 wt.% of the mixture, leading to an increase in the hole mobility. This behavior is in stark contrast to mixtures of the archetypical small molecule D-A system of CuPc-C_{60}, where the hole mobility decreases with increasing C_{60} composition, while the electron mobility is noted to increase.[24] As a result, the optimum composition is ~50 wt.%, where both the electron and hole mobility are simultaneously maximized. The difference between the CuPc:C_{60} and SubPc:C_{60} systems arises from a difference in donor crystallinity. Neat CuPc is polycrystalline, and the addition of 25 wt.% C_{60} results in an amorphous mixture.[24] This loss of crystallinity leads to a reduction in the hole mobility with increasing C_{60} composition.[24] For SubPc:C_{60} OPVs containing an optimized mixture, a maximum power conversion efficiency of $\eta_P = (3.7 \pm 0.1)\%$ is realized compared to $\eta_P = (3.0 \pm 0.1)\%$ obtained for a planar heterojunction cell at 100 mW cm^{-2} under simulated AM1.5G solar illumination. Here, the formation of nanocrystalline domains of SubPc in C_{60}-rich mixtures makes it possible to realize high exciton diffusion efficiency combined with a high charge collection efficiency. An improved understanding of the crystallization behavior of SubPc:C_{60} may ultimately permit additional improvements in device performance for this system, and other phthalocyanine systems of interest for OPVs.

4. Experimental Section

Device Fabrication: Organic photovoltaic cells were fabricated on glass substrates pre-coated with indium-tin-oxide (ITO) having a sheet resistance of 15 Ω per square. The substrates were cleaned in tergitol solution and in organic solvents, before being exposed to a UV-ozone treatment for 5 min.. Boron subphthalocyanine chloride (Rubipy Scientific Inc., ~99% purity) and C_{60} (MER Corporation, ~99.9% purity) were used as the donor and acceptor materials, respectively. The organic layers and Al cathode were deposited by vacuum thermal evaporation at a base pressure $<8 \times 10^{-7}$ Torr. All organic layers were deposited at a total rate of 0.2 nm s^{-1}. A 10-nm-thick layer of molybdenum oxide (MoO_3) was included on top of the ITO anode in both planar and optimized mixed (Figure 2 and Figure 3) OPVs.[29] In addition, a 10-nm-thick layer of bathocuproine (BCP) was used as an exciton blocking layer in all OPVs.[28] An Al cathode was deposited at a rate of 0.3 nm s^{-1} through a shadow mask defining an active area that is 1 mm in diameter. The optimized planar heterojunction OPV used for comparison consists of a 13-nm-thick layer of SubPc and a 35-nm-thick layer of C_{60}. For hole-only devices, an ITO anode and a 35-nm-thick Au cathode were used to extract the hole mobility from uniform mixtures of SubPc and C_{60}. For measurements of the electron mobility, mixed films were sandwiched between a 50-nm-thick Al anode and 1-nm-thick LiF/50-nm-thick Al cathode.

Device Characterization: Electrical characterization was performed in air immediately after device fabrication in the dark and under simulated AM1.5G solar irradiance using a 150 W Oriel solar simulator. Current–voltage characteristics were measured using an Agilent Technologies 4155C semiconductor parameter analyzer as a function of illumination intensity, which was varied using neutral density filters. The optical power was measured using a Newport 818P-010-12 high-power detector. The external quantum efficiency (η_{EQE}) was measured under monochromatic light generated from a Xe lamp attached to a monochromator. Photocurrent measurements at each wavelength were made using a lock-in amplifier. The J_{SC} value as derived from the integrated η_{EQE} spectrum is within 10% of the J_{SC} value measured under simulated AM1.5G solar illumination at 100 mW cm^{-2}.

Absorbance: Absorption spectra for organic films grown on glass substrates were collected using a OLIS Cary-14 spectrophotometer.

XRD: X-ray diffraction measurements were performed using a microdiffractometer in the θ–2θ geometry using Cu Kα radiation. All organic films were grown on a Si (111) substrate covered with native oxide.

TEM: Lacey carbon grids coated with a ~5-nm-thick carbon layer were used as the substrates for obtaining transmission electron microscopy (TEM) plane-view images. The microscope is an FEI Tecnai G2 F30 (S) TEM at the University of Minnesota, operated at 200 kV.[47] All images were filtered to enhance visibility. For selected-area electron diffraction (SAED), a region 5 µm in diameter was selected by the aperture. For SAED, a beam energy of 300 keV was used. No substantial beam damage was observed during TEM imaging. All organic layers were 60-nm-thick to correlate with optimum device thicknesses.

Role of the Substrate: Different substrates were chosen for various characterization techniques due to experimental constraints involved. However, we have worked to ensure that the correlations observed between structure, charge transport, and device performance are valid by examining the role of substrate choice in these measurements. Identical hole mobility values were measured using ITO substrates both with and without an MoO_3 interlayer, suggesting that there is no change in bulk transport upon including the MoO_3 layer. Rigorous TEM imaging was carried out both on Si (single crystal) substrates and carbon-grids (amorphous). Similar morphology was observed in both cases again confirming that the growth of nanocrystalline SubPc domains is independent of the underlying substrate.

Acknowledgements

This work was supported by the National Science Foundation (NSF) under Award Number CBET-0946723 and the NSF MRSEC Program under Award Number DMR-0819885. Support was also received from the University of Minnesota Initiative for Renewable Energy and the Environment. Parts of this work were carried out in the Characterization Facility, University of Minnesota, which receives partial support from NSF through the MRSEC program.

Received: August 18, 2011
Revised: October 18, 2011

---

[1] S. E. Shaheen, D. S. Ginley, G. E. Jabbour, *MRS Bull.* **2005**, *30*, 10.
[2] R. Gaudiana, C. Brabec, *Nat. Photon.* **2008**, *2*, 287.
[3] B. A. Gregg, *J. Phys. Chem. B* **2003**, *107*, 4688.

[4] Y. Liang, Z. Xu, J. Xia, S.-T. Tsai, Y. Wu, G. Li, C. Ray, L. Yu, *Adv. Mater.* **2010**, *22*, E135.
[5] S. H. Park, A. Roy, S. Beaupré, S. Cho, N. Coates, J. S. Moon, D. Moses, M. Leclerc, K. Lee, A. J. Heeger, *Nat. Photon.* **2009**, *3*, 297.
[6] G. Li, V. Shrotriya, J. Huang, Y. Yao, T. Moriarty, K. Emery, Y. Yang, *Nat. Mater.* **2005**, *4*, 864.
[7] K. Kim, J. Liu, M. A. G. Namboothiry, D. L. Carroll, *Appl. Phys. Lett.* **2007**, *90*, 163511-1.
[8] D. Gebeyehu, B. Maennig, J. Drechsel, K. Leo, M. Pfeiffer, *Sol. Energy Mater. Sol. Cells* **2003**, *79*, 81.
[9] F. Yang, K. Sun, S. R. Forrest, *Adv. Mater.* **2007**, *19*, 4166.
[10] S. Heutz, P. Sullivan, B. M. Sanderson, S. M. Schultes, T. S. Jones, *Sol. Energy Mater. Sol. Cells* **2004**, *83*, 229.
[11] T. Tsuzuki, Y. Shirota, J. Rostalski, D. Meissner, *Sol. Energy Mater. Sol. Cells* **2000**, *61*, 1.
[12] G. Wei, S. Wang, K. Sun, M. E. Thompson, S. R. Forrest, *Adv. Energy Mater.* **2011**, *1*, 184.
[13] P. Peumans, S. Uchida, S. R. Forrest, *Nature* **2003**, *425*, 158.
[14] Y. Zheng, S. K. Pregler, J. D. Myers, J. Ouyang, S. B. Sinnott, J. Xue, *J. Vac. Sci. Technol. B* **2009**, *27*, 169.
[15] B. Walker, A. B. Tamayo, X.-D. Dang, P. Zalar, J. H. Seo, A. Garcia, M. Tantiwiwat, T.-Q. Nguyen, *Adv. Funct. Mater.* **2009**, *19*, 3063.
[16] K. L. Mutolo, E. I. Mayo, B. P. Rand, S. R. Forrest, M. E. Thompson, *J. Am. Chem. Soc.* **2006**, *128*, 8108.
[17] H. Gommans, D. Cheyns, T. Aernouts, C. Girotto, J. Poortmans, P. Heremans, *Adv. Funct. Mater.* **2007**, *17*, 2653.
[18] P. Sullivan, A. Duraud, I. Hancox, N. Beaumont, G. Mirri, J. H. R. Tucker, R. A. Hatton, M. Shipman, T. S. Jones, *Adv. Energy Mater.* **2011**, *1*, 352.
[19] D. Cheyns, B. P. Rand, P. Heremans, *Appl. Phys. Lett.* **2010**, *97*, 033301-1.
[20] R. R. Lunt, N. C. Giebink, A. A. Belak, J. B. Benziger, S. R. Forrest, *J. Appl. Phys.* **2009**, *105*, 053711-1.
[21] W. A. Luhman, R. J. Holmes, *Adv. Funct. Mater.* **2011**, *21*, 764.
[22] S. Uchida, J. Xue, B. P. Rand, S. R. Forrest, *Appl. Phys. Lett.* **2004**, *84*, 4218.
[23] M. Hiramoto, H. Fujiwara, M. Yokoyama, *Appl. Phys. Lett.* **1991**, *58*, 1062.
[24] B. P. Rand, J. Xue, S. Uchida, S. R. Forrest, *J. Appl. Phys.* **2005**, *98*, 124902-1.
[25] M. Brönner, A. Opitz, W. Brütting, *Phys. Stat. Sol. A* **2008**, *205*, 549.
[26] J. Xue, B. P. Rand, S. Uchida, S. R. Forrest, *J. App. Phys.* **2005**, *98*, 124903-1.
[27] R. Pandey, R. J. Holmes, *IEEE J. Sel. Top. Quant. Elec.* **2010**, *16*, 1537.
[28] B.P. Rand, J. Li, J. Xue, R. J. Holmes, M. E. Thompson, S. R. Forrest, *Adv. Mater.* **2005**, *17*, 2714.
[29] R. Pandey, R. J. Holmes, *Adv. Mater.* **2010**, *22*, 5301.
[30] M. Kröger, S. Hamwi, J. Meyer, T. Riedl, W. Kowalsky, A. Kahn, *Appl. Phys. Lett.* **2009**, *95*, 123301.
[31] H. Benten, M. Ogawa, H. Ohkita, S. Ito, *Adv. Funct. Mater.* **2008**, *18*, 1563.
[32] G. Ruani, C. Fontanini, M. Murgia, C. Taliani, *J. Chem. Phys.* **2002**, *116*, 1713.
[33] W. A. Luhman, R. J. Holmes, *Appl. Phys. Lett.* **2009**, *94*, 153304-1.
[34] P. Peumans, A. Yakimov, S. R. Forrest, *J. App. Phys.* **2003**, *93*, 3693.
[35] M. A. Lampert, P. Mark, *Current Injection in Solids*, Academic Press, New York **1970**.
[36] V. D. Mihailetchi, L. J. A. Koster, P. W. M. Blom, C. Melzer, B. de Boer, J. K. J. van Duren, R. A. J. Janssen, *Adv. Funct. Mater.* **2005**, *15*, 795.
[37] S. M. Tuladhar, D. Poplavskyy, S. A. Choulis, J. R. Durrant, D. D. C. Bradley, J. Nelson, *Adv. Funct. Mater.* **2005**, *15*, 1171.
[38] J. Frenkel, *Phys. Rev.* **1938**, *54*, 647.
[39] P. W. M. Blom, M. J. M. de Jong, M. G. van Munster, *Phys. Rev. B* **1997**, *55*, 656.
[40] D. H. Dunlap, V. M. Kenkre, P. E. Parris, *J. Imaging Sci. Technol.* **1999**, *43*, 437.
[41] S. V. Rakhmanova, E. M. Conwell, *Appl. Phys. Lett.* **2000**, *76*, 3822.
[42] A. Opitz, M. Brönner, J. Wagner, M. Götzenbrugger, W. Brütting, *Proc. SPIE* **2008**, *7002*, 70020J.
[43] Z. R. Hong, B. Maennig, R. Lessmann, M. Pfeiffer, K. Leo, P. Simon, *Appl. Phys. Lett.* **2007**, *90*, 203505.
[44] T. Itoh, S. Nitta, S. Nonomura, *Appl. Surf. Sci.* **1997**, *113/114*, 282.
[45] C. C. Mattheus, W. Michaelis, C. Kelting, W. S. Durfee, D. Wohrle, D. Schlettwein, *Synth. Met.* **2004**, *146*, 335.
[46] H. Kietaibl, *Monatshefte Chem.* **1974**, *105*, 405.
[47] M. J. Behr, K. A. Mkhoyan, E. S. Aydil, *ACS Nano* **2010**, *4*, 5087.